ACSNANO

www.acsnano.org

Crossover from 2D Ferromagnetic Insulator to Wide Band Gap Quantum Anomalous Hall Insulator in Ultrathin $MnBi_2Te_4$

Chi Xuan Trang,[#] Qile Li,[#] Yuefeng Yin,[#] Jinwoong Hwang, Golrokh Akhgar, Iolanda Di Bernardo, Antonija Grubišić-Čabo, Anton Tadich, Michael S. Fuhrer, Sung-Kwan Mo, Nikhil V. Medhekar,* and Mark T. Edmonds*

Cite This: *ACS Nano* 2021, 15, 13444−13452

Read Online

ACCESS | Metrics & More | Article Recommendations | Supporting Information

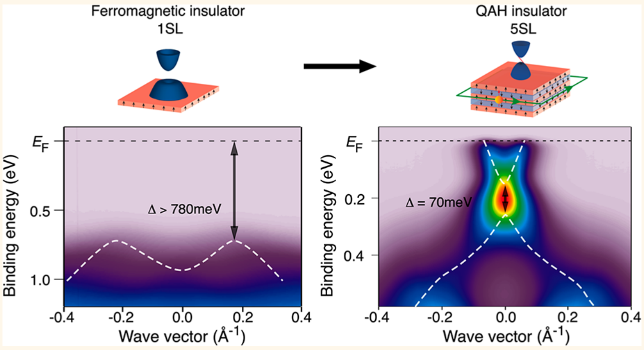

ABSTRACT: **Intrinsic magnetic topological insulators offer low disorder and large magnetic band gaps for robust magnetic topological phases operating at higher temperatures. By controlling the layer thickness, emergent phenomena such as the quantum anomalous Hall (QAH) effect and axion insulator phases have been realized. These observations occur at temperatures significantly lower than the Néel temperature of bulk $MnBi_2Te_4$, and measurement of the magnetic energy gap at the Dirac point in ultrathin $MnBi_2Te_4$ has yet to be achieved. Critical to achieving the promise of this system is a direct measurement of the layer-dependent energy gap and verification of a temperature-dependent topological phase transition from a large band gap QAH insulator to a gapless TI paramagnetic phase. Here we utilize temperature-dependent angle-resolved photoemission spectroscopy to study epitaxial ultrathin $MnBi_2Te_4$. We directly observe a layer-dependent crossover from a 2D ferromagnetic insulator with a band gap greater than 780 meV in one septuple layer (1 SL) to a QAH insulator with a large energy gap (>70 meV) at 8 K in 3 and 5 SL $MnBi_2Te_4$. The QAH gap is confirmed to be magnetic in origin, as it becomes gapless with increasing temperature above 8 K.**

KEYWORDS: *magnetic topological insulator, thin film, $MnBi_2Te_4$, quantum anomalous Hall insulator, ferromagnetic insulator, angle-resolved photoemission spectroscopy*

INTRODUCTION

Topological insulators (TIs) in three dimensions possess a topologically protected spin-polarized gapless Dirac cone on the surface of a bulk insulator that is robust against time-reversal invariant perturbations.[1−7] Time-reversal symmetry in TIs can be broken by introducing long-range magnetic order, resulting in profound changes to the electronic band structure, specifically a gap opening at the Dirac point caused by exchange coupling.[6,8−10] The combination of magnetization and strong spin−orbit coupling in ultrathin topological insulators not only results in a gap opening but also the presence of chiral edge modes within the magnetic gap representing the quantum anomalous Hall (QAH) insulating state.[9−11] In this state the edge mode is chiral and perfectly spin-polarized, yielding dissipationless transport of charge with applications in spintronic and ultralow energy electronics.[12] Furthermore, a realization of distinct topological phases based on broken time-reversal symmetry such as the chiral Majorana fermion[13] and axion insulator states are also achievable.[14,15]

The QAH effect was first realized via dilute magnetic doping using Cr and V in ultrathin films of $(Bi,Sb)_2Te_3$.[9,10] However, the nonuniform doping and magnetization result in large spatial fluctuations in the size of the magnetic gap,[16] and the parallel dissipative channels create spin-scattering which greatly suppresses the temperature at which QAH effect (QAHE) can be observed. Modulation-doped sandwich heterostructures have modestly raised the QAHE temperature to 1−2 K,[17,18] which is still far below the size of the magnetic gap and the Curie

Received: May 9, 2021
Accepted: August 2, 2021
Published: August 13, 2021

https://doi.org/10.1021/acsnano.1c03936
ACS Nano 2021, 15, 13444−13452

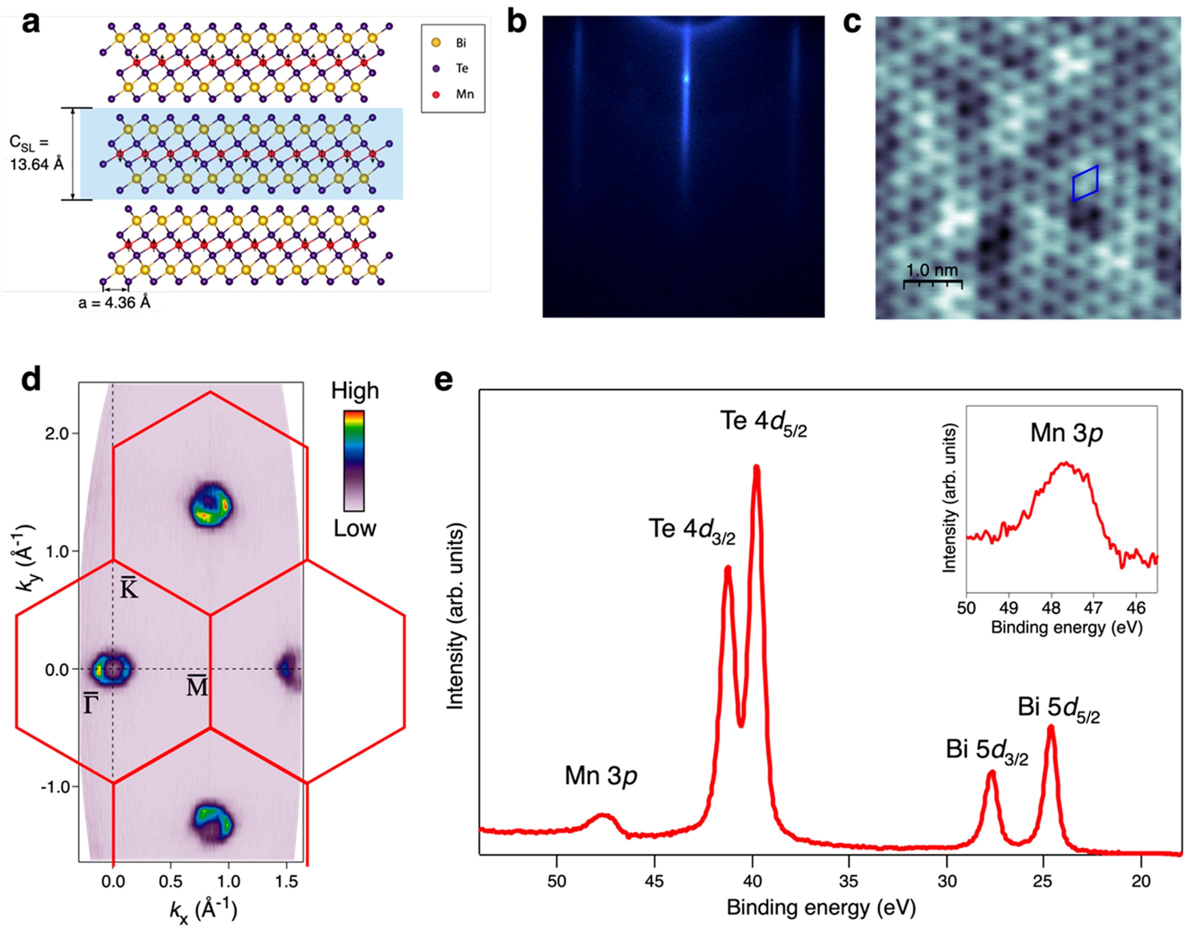

Figure 1. Basic properties and characterization of $MnBi_2Te_4$. (a) Layered crystal structure of $MnBi_2Te_4$. (b) Reflection high-energy electron diffraction (RHEED) of 3 SL $MnBi_2Te_4$ along the [11-2] direction. (c) Atomic-resolution scanning tunnelling microscope (STM) (5nm × 5nm) image of $MnBi_2Te_4$ ($V = -2.7$ V, $I = 70$ pA) showing the 1 × 1 structure (blue diamond). Lattice constant is 0.43 nm. (d) Constant-energy angle-resolved photoemission spectroscopy (ARPES) contour of 2 SL $MnBi_2Te_4$ measured with $h\nu$ = 63eV taken at the Fermi level over multiple Brillouin zones (BZ). Hexagonal BZ is overlaid in red. (e) Core-level spectrum of $MnBi_2Te_4$ taken at $h\nu$ = 1486 eV showing the characteristic Mn 3p, Te 4d, and Bi 5d core levels.

temperature. To explore the QAHE and other topological phases at elevated temperatures requires uniform distribution of magnetization, which is not readily achieved via dilute magnetic doping.

The intrinsic magnetic topological insulator $MnBi_2Te_4$ was recently proposed[19−22] and experimentally verified as a bulk antiferromagnetic topological insulator[23−26] that hosts both intrinsic magnetism and topological protection. $MnBi_2Te_4$ is a layered compound similar to the well-known TI Bi_2Te_3, where five atomic layers of Te−Bi−Te−Bi−Te form a quintuple layer (QL); however, $MnBi_2Te_4$ has an extra Mn−Te layer in between Te and Bi in the middle of the Bi_2Te_3 quintuple layer, forming a septuple layer (SL) (Figure 1a). The origin of the magnetic order comes from the Mn^{2+} ions (contributing a 5 μ_B magnetic moment), with moments coupled ferromagnetically within each SL and antiferromagnetically between adjacent SLs, resulting in an uncompensated antiferromagnet. By controlling the layer structure in the 2D limit, a set of thickness-dependent magnetic and topological transitions have been predicted, such as a wide band gap ferromagnetic (FM) insulator in 1 SL with potential applications in proximity-induced magnetization.[21] Beyond 1 SL, even- and odd-layered systems are predicted to be axion insulators and wide band gap QAH insulators, respectively.[19,22] Recent transport experiments on $MnBi_2Te_4$ have confirmed the axion insulator phase in 6 SL[15] and the QAHE in 5 SL at 1.4 K at zero magnetic field, further increased to 6.5 K in an external magnetic field by aligning the layers ferromagnetically,[27] yet these temperatures correspond to thermal energies of <1 meV and are still well below the predicted magnetic band gap values (ranging between 38 meV[19] and 98 meV)[27] and below the Néel temperature ($T_N \approx 23-25$ K).[25,27] To date, the electronic band structure of ultrathin $MnBi_2Te_4$ has only been examined above the Néel temperature where it appears gapless.[28] Hence, neither direct confirmation of the crossover from ferromagnetic (FM) insulator to QAH insulator with increasing layer thickness nor direct observation of the size or magnetic nature of the energy gap in the QAH state has been found.

In this work, we precisely control the layer thickness of $MnBi_2Te_4$ via molecular beam epitaxy (MBE) growth and perform temperature-dependent angle-resolved photoemission spectroscopy (ARPES) above and below the Néel temperature to reveal the layer-dependent crossover from 2D ferromagnetic insulator (Δ_{GAP} > 780 meV) in 1 SL to a QAH insulator with large gaps (Δ > 70 meV at 8 K) in 3 and 5 SL, in excellent agreement with first-principles density functional theory (DFT) calculations. The QAH gap is confirmed to be magnetic in origin, as it abruptly becomes zero with increasing temperature as the system becomes paramagnetic, demonstrating a phase

Table 1. Lattice Constant, Band Gap, and Fermi Velocity as a Function of the Thickness of $MnBi_2Te_4$

		E_g (meV)		ν_F (m/s)	
	lattice constant, a (Å)	theory	experiment	hole	electron
1 SL	4.06 ± 0.30	550 [this work] 700 [ref 19] 321 [ref 22]	>780 ± 100		
2 SL	4.31 ± 0.30	200 [this work] 107 [ref 22]	300 ± 100		
3 SL	4.31 ± 0.30	125 [this work] 66 [ref 22]	109 ± 15 (hyperbolic model) 71 ± 15 (EDC model)	$2.0 \pm 0.5 \times 10^5$	$4.2 \pm 0.5 \times 10^5$
5 SL	4.31 ± 0.30	38 [ref 19] 77 [ref 22] 98 [ref 27]	84 ± 15 (hyperbolic model) 70 ± 15 (EDC model)	$2.9 \pm 0.5 \times 10^5$	$5.0 \pm 0.5 \times 10^5$

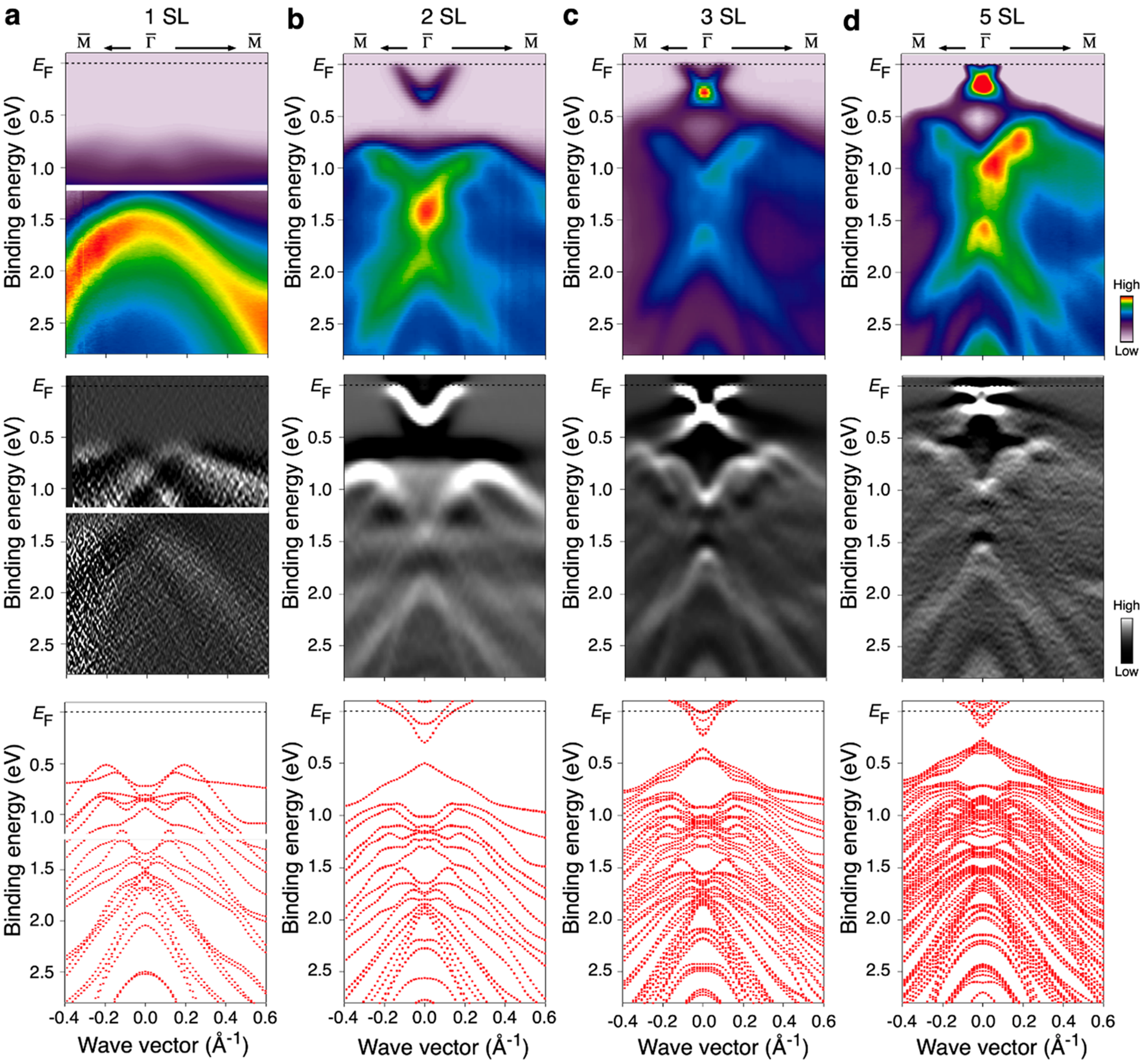

Figure 2. Thickness dependence of the band structure of $MnBi_2Te_4$ and comparison with calculation. ARPES intensity (top), double derivatives (middle), and DFT calculation (bottom) of (a) 1 SL; (b) 2 SL; (c) 3 SL; and (d) 5 SL along the $\overline{\Gamma M}$ cut, measured at $h\nu = 50$ eV and $T = 13$ K.

transition from a QAH insulating state to a topological gapless surface state.

RESULTS AND DISCUSSION

High-quality $MnBi_2Te_4$ films were grown by molecular beam epitaxy on Si(111)-7 × 7 substrates via alternately growing 1 QL Bi_2Te_3 and 1 bilayer MnTe to spontaneously form $MnBi_2Te_4$ (see the "Methods" section for specific details on the growth). Figure 1b shows a reflection high-energy electron diffraction (RHEED) pattern of 3 SL $MnBi_2Te_4$. The atomically flat morphology of the film is indicated by a sharp (1 × 1) streak pattern (see Supporting Information Section 1 for LEED and

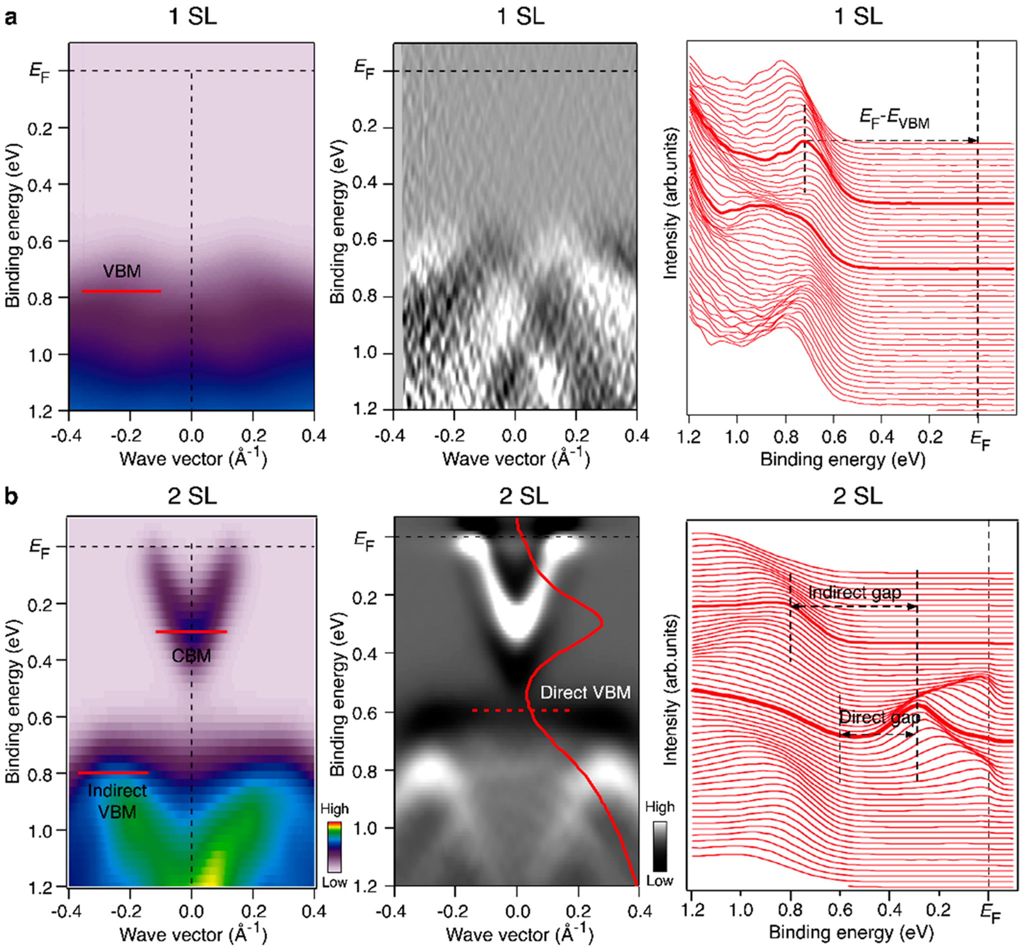

Figure 3. Band gap of 1 and 2 SL $MnBi_2Te_4$. Near E_F ARPES intensity (left) at $h\nu$ = 50 eV and T = 12 K, double derivatives (middle), and corresponding energy distribution curves (EDCs) (right) around the $\bar{\Gamma}$ point for (a) 1 SL, and (b) 2 SL. The VB maximum and CB minimum are marked as red lines in ARPES intensity.

additional RHEED data). Figure 1c shows an atomic-resolution scanning tunneling microscopy (STM) image and the expected 1 × 1 atomic structure with a lattice constant of 4.3 Å. A constant binding energy ARPES map taken at the Fermi level (i.e., Fermi surface map) of 2 SL $MnBi_2Te_4$, capturing multiple Brillouin zones (BZ) is shown in Figure 1d. In each BZ, the only features observed are at the $\bar{\Gamma}$ points, showing a slight hexagonal warping of the Fermi surface. The hexagonal features confirm 3-fold rotational symmetry, consistent with the rhombohedral structure of $MnBi_2Te_4$. An in-plane lattice constant, $a \approx 4.3$ Å, can be calculated from the Fermi surface map for 2 SL, with similar values for 3 and 5 SL (see Supporting Information Section 2) in excellent agreement with STM (Figure 1c) and previous reports on bulk $MnBi_2Te_4$.[26,29] In contrast, 1 SL has a lattice constant of 4.06 Å suggesting there is the compressive strain when in direct contact with the Si(111), immediately relaxed when the thickness increases. These results are summarized in Table 1. Figure 1e shows X-ray photoelectron spectroscopy (XPS) data of 5 SL taken at $h\nu$ = 1486 eV, with the characteristic Mn 3p, Te 4d, and Bi 5d core levels observed in the correct chemical stoichiometry when accounting for the different photoionization cross sections. Depth-dependent XPS measurements are shown in Figure S3 to demonstrate that the films are composed of solely $MnBi_2Te_4$ and not a composition of Bi_2Te_3 with MnTe on the top.

By delicate control of the growth conditions, we achieve SL-by-SL growth of $MnBi_2Te_4$, allowing the DFT-predicted transition from ferromagnetic insulator to quantum anomalous Hall insulator to be probed directly with ARPES. The upper panel of Figure 2 shows a series of ARPES band maps of $MnBi_2Te_4$ with thicknesses of (a) 1 SL, (b) 2 SL, (c) 3 SL and (d) 5 SL measured along the $\bar{\Gamma}\bar{M}$ direction. The middle panel in Figure 2 plots the respective double derivative, and the bottom panel plots the corresponding DFT calculations using HSE functional (1−3 SL) and PBE functional (5 SL). There is a clear thickness-dependent transition from a wide band gap in 1 SL (Figure 2a) to an evolution into nearly Dirac-like dispersion in 3 and 5 SL (Figure 2c,d), evidence of evolution toward nontrivial topological features. There is an excellent overlap with the DFT calculations in the overall band shape and with increasing thickness, along with a rigid shift in the bands toward the Fermi level, suggesting that the film becomes less n-type due to increased manganese content which acts as a hole dopant.[6]

In Figure 3a,b, we determine the band gap in 1 and 2 SL $MnBi_2Te_4$, respectively, by plotting the ARPES spectrum (left panel), its double derivative (middle panel), and the corresponding energy distribution curves (right panel). In Figure 3a, the ARPES spectrum of 1 SL $MnBi_2Te_4$ exhibits only a broad M-shaped valence band (VB), with the VB maximum ≈780 meV below the Fermi level, with no signature of the conduction band (CB) and a strong intensity bulk Si(111) band

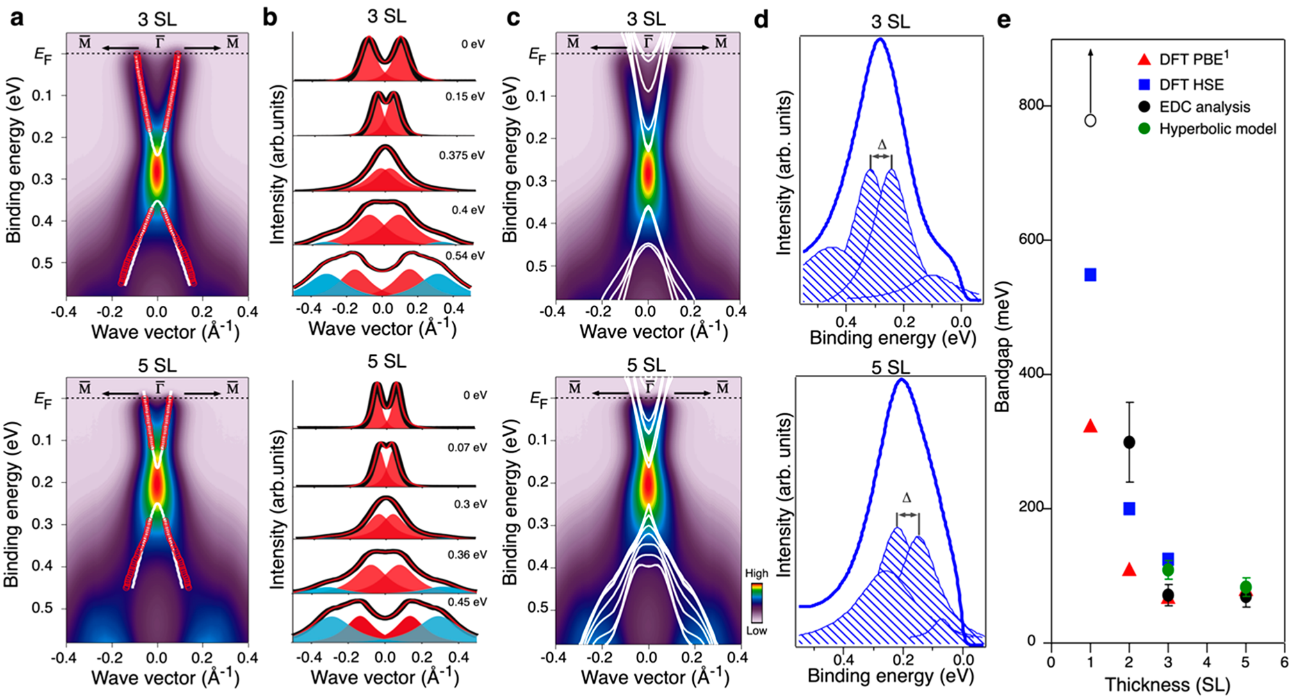

Figure 4. Magnetic gap of 3 and 5 SL $MnBi_2Te_4$. High-resolution ARPES intensity of 3 SL (top) and 5 SL (bottom) taken at $h\nu$ = 50 eV and T = 8 K with overlaid (a) hyperbolic band fittings (white lines) with extracted momentum distribution curve (MDC) peak maxima (red circles). (b) MDCs at different E_B fit with Lorentzian line shapes. (c) DFT calculations overlaid on the ARPES data. (d) EDC spectra taken at $k_{\|}$ = 0. The splitting of the two main peak line shapes corresponds to the magnetic gap, Δ. (e) Band gap as a function of thickness including data from experiment (black), fittings from hyperbolic model (green), DFT calculation (blue), and Otrokov et al.[22] (red). The open circle for 1 SL reflects only $E_F - E_{VBM}$ and not the band gap as the conduction band is not observed below the Fermi level.

observed below 1.1 eV. The overall band shape confirms an indirect band gap ferromagnetic insulator in excellent agreement with our DFT results and ref 22. This is different from that reported by ref 19, which reports a direct band gap, which is likely as a result of applying the on-site Hubbard correction term to Te instead of Mn (further discussion and calculations are found in Supporting Information Section S4). The gap of >780 meV is larger than theoretical predictions (see Table 1) and is either due to band gap underestimation in DFT[30] or the compressive strain that is observed in 1 SL. The gap size is comparable to other 2D ferromagnets, such as monolayer CrI_3,[31] but it is significantly larger than that in (nonmagnetic) 1 QL pristine Bi_2Te_3.[4] In Figure 3b for the 2 SL film, the M-shaped VB is preserved, but now a parabolic CB appears whose minimum is below E_F, indicating that the film is n-type doped. The CB dispersion within a 0.15 Å^{-1} region extending from the $\bar{\Gamma}$ point is fit using a nearly free electron model, $E = \hbar^2k^2/2m^*$, yielding an effective mass $m^* = 0.25m_0$ (see Supporting Information Section S5 and Figure S7 for fits). An extremely weak intensity hole band, only observable when taking a double derivative (middle panel of Figure 3b), results in a direct band gap of 300 ± 100 meV. The excellent agreement with DFT suggests that 2 SL is a zero plateau QAH insulator.[22]

We now examine the size of the band gap in 3 and 5 SL $MnBi_2Te_4$. Figure 4a shows high-resolution ARPES maps taken at $h\nu$ = 50 eV and 8 K (i.e., well below the Néel temperature, T_N ≈ 23−25 K[25,27]) for 3 SL (top panel) and 5 SL (bottom panel). The red circles overlaid reflect the extracted maxima from fitting momentum distribution curves (MDC) with Lorentzian line shapes in the k range between −0.5 to +0.5 Å^{-1} as shown in Figure 4b. Fitting with four-line shapes was used for binding energies below ∼0.4 and ∼0.3 eV for 3 and 5 SL, respectively, in order to decouple the linearly dispersing Dirac bands from additional VBs which are clearly present in the MDCs in Figure 4b and predicted in the DFT calculations in Figure 4c. These additional bands when interacting with the Dirac hole band lead to an anticrossing and manifest as a slight kink in the band dispersion. The strong spectral weight near $\bar{\Gamma}$ in the Dirac point region is due to Te-orbital-related matrix element effects (see Figure S6 for orbital character analysis) as this intensity diminishes quickly with changing photon energy (see Figure S8). This strong spectral weight has previously been observed in the Dirac point region of Bi_2Te_3[3] and $Bi_2Te_3/MnBi_2Te_4$ heterostructures, but not in Mn-doped Bi_2Se_3.[7] A clear electron and hole band asymmetry is observed, yielding asymptotic Fermi velocities for 3 SL of $\nu_{F,e} \approx 4.2 \times 10^5$ ms^{-1} and $\nu_{F,h} \approx 2.0 \times 10^5$ ms^{-1} and for 5 SL $\nu_{F,e} \approx 5.0 \times 10^5$ ms^{-1} and $\nu_{F,h} \approx 2.9 \times 10^5$ ms^{-1}. The hole band ν_F for both 3 and 5 SL was extracted above the kink regions discussed above.

The band dispersion for both 3 and 5 SL appear hyperbolic, as expected for a massive Dirac dispersion, and the linear extrapolation of the electron and hole bands to k = 0 shows the bands do not meet at a discreet point (i.e., the Dirac point) but are actually separated by 40 ± 15 meV for both 3 and 5 SL $MnBi_2Te_4$. This strongly supports the conclusion that the system is gapped, and in order to accurately determine the size of the band gap, we utilize two independent methods. The first is based on the hyperbolic band dispersion for both 3 and 5 SL as expected for a massive Dirac dispersion, so we fit the data to a model of a hyperbolic system (shown as white bands in Figure 4a) given by

$$E_i(k) = D \pm \sqrt{\Delta_i^2 + \hbar^2 \nu_{F,i}^2 (k + k_0)^2} \quad i \in n, p \tag{1}$$

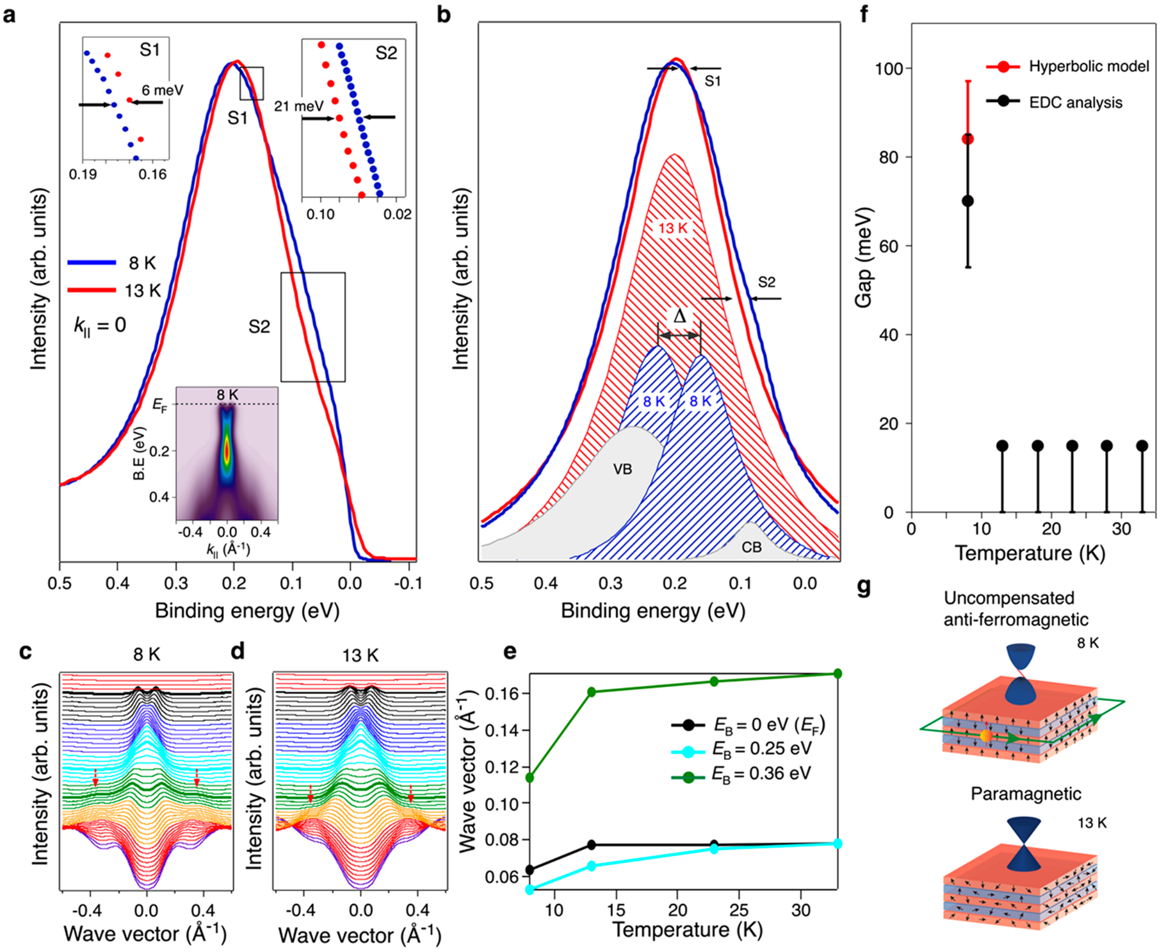

Figure 5. Temperature dependence of 5 SL film. (a) Energy distribution curves (EDCs) taken at $k_{||} = 0$ taken at 8 and 13 K for 5 SL $MnBi_2Te_4$. The regions S1 and S2 indicate a clear broadening and pronounced shoulder at 8 K, corresponding to a splitting of 6 and 27 meV, respectively. The inset in (a) shows the ARPES map taken at 8 K. (b) Simulated peak fitting results from the spectra in (a), corresponding to a magnetic gap of 70 ± 15 meV at 8 K and 15 ± 15 meV at 13 K. (c, d) MDCs with different colors designating different binding energy regions for 3 and 5 SL respectively. E_F: black: 0.09 eV, blue: 0.1−1.9 eV, sky blue: 0.2−0.29 eV, green: 0.3−0.39 eV, orange: 0.4−0.49 eV, red: 0.5−0.59 eV, purple: 0.6−0.62 eV. (e) Wave vector, k, extracted from MDC peak maxima as a function of temperature at $E_B = 0$ (black), 0.25 (blue), and 0.36 eV (green) showing a clear band evolution with increasing temperature. (f) Band gap as a function of temperature. (g) Schematics of uncompensated antiferromagnetism QAH insulator phase (upper) and paramagnetic gapless TI phase (lower).

where $\Delta_i = \Delta_n + \Delta_p$ represents the band gap, D is the doping, and $\nu_{F,i}$ is the asymptotic Fermi velocities away from the gapped region at large momenta. This yields magnetic gap sizes of $\Delta_{3SL} = 109 \pm 15$ meV and $\Delta_{5SL} = 84 \pm 15$ meV. Figure 4c overlays the DFT band calculations and shows excellent overlap for 3 SL, while the 5 SL PBE (due to underestimation of the band gap)[30] required the band gap to be adjusted to match the experimental data using the scissors method.

A check on the determination of the band gap was carried out by peak fitting analysis of the energy distribution curves (EDCs) taken at $k_{||} = 0$. The EDCs for 3 and 5 SL $MnBi_2Te_4$ taken at 8 K are plotted in Figure 4d, along with the peak fitting analysis based on ref 7 for $Bi_2Te_3/MnBi_2Te_4$ heterostructures where a pronounced shoulder is observed when cooling below 13 K (the temperature dependence and the evolution of electronic structure is shown in Figure 5 and discussed in detail below). We fit the dominant spectral weight with two identical Lorentzian line shapes and include small additional CB and VB peaks on either side of the main peaks that reflect the electron and hole Dirac bands. At 8 K we arrive at gaps for 3 and 5 SL of 71 ± 15 meV and 70 ± 15 meV, respectively. In Figure S11, we include fits of the 8 K data with (a) four peaks to reflect a gapped system and (b) three peaks to reflect a gapless system with only a single main Dirac peak. The three peaks fit is unable to reproduce the shoulder on the right flank of the peak in the experimental data, validating our four peak fitting approach. The band gap derived from EDC fitting using four peak components shows excellent agreement with that obtained from fitting to eq 1 for 5 SL $MnBi_2Te_4$ and a slight discrepancy above experimental error for 3 SL. Figure 4e plots the band gap as a function of thickness for experiment and DFT calculations from this work and that of ref 22 and are also summarized in Table 1.

We now investigate the response of the topological electronic structure to magnetic ordering, by conducting temperature-dependent ARPES measurements. Figure 5a shows the energy distribution curves at $k_{||} = 0$ measured at temperatures $T = 8$ and 13 K for 5 SL $MnBi_2Te_4$. There is a clear broadening upon cooling from 13 K, and the right flank of the peak (i.e., lower binding energy) develops a clear shoulder. Higher temperature measurements (up to 33 K) show a minimal change from the 13 K data, which suggests that 8 K is below the magnetic phase transition temperature, i.e., uncompensated antiferromagnetic phase (uAFM), and 13 K above it, i.e., paramagnetic phase. In Figure 5b, we fit the $T = 13$ K spectra (fitting up to 33 K was also carried out) with two almost identical components yielding a splitting of 15 meV. Figure S11 shows a comparison between fitting with (c) two peaks and (d) on peak component at 13 K. A slightly larger peak intensity for the hole band was adopted due to the lower Fermi velocity of the hole band. This splitting of less than 15 meV reflects a nearly gapless topological insulator (that maintains a small remnant confinement gap due to its ultrathin nature) confirming the system is now paramagnetic. The sum of these two peaks is plotted as a single peak component (red line shape) for clarity in Figure 5b. Upon cooling to 8 K and the uAFM phase, the peak splitting of these two components (blue line shapes) increases and yields a magnetic gap, $\Delta = 70 \pm 15$ meV.

There is further evidence of a band evolution between 8 and 13 K when examining the near-E_F ARPES maps and the corresponding MDCs at 8 K (Figure 5c) and 13 K (Figure 5d; the full temperature range 8−33 K is shown in Figure S9). As shown in Figure 5e at binding energies $E_B = 0$, 0.25, and 0.36 eV, there is a clear increase in wavevector, k with increasing T. However, the slope of the electron and hole bands (and consequently Fermi velocity) extracted from the MDC maxima remains unchanged as shown in Figure S9c. At 13 K and above, linear extrapolation of the bands to $k = 0$ yields a gap $\Delta < 10$ meV in excellent agreement with the EDC analysis above. The near gapless nature at 13 K and above is further confirmed via ARPES measurements taken at $T = 13$ K and $h\nu = 40$ eV (shown in Figure S10) in order to avoid the strong spectral weight of the Te orbital in the gapped region. This clearly shows a gapless Dirac dispersion and is consistent with measurements taken of 5 and 7 SL $MnBi_2Te_4$ at 25 K in ref 28. Figure 5f plots the band gap as a function of temperature.

This clear emergence of a magnetization-induced gap with decreasing temperature provides a definitive signature for a temperature-dependent topological phase transition from a large band gap QAH insulator to a near gapless TI paramagnetic phase. These phases are depicted schematically in Figure 5g. It should be noted that the phase transition temperature reported here between 8 and 13 K is well below the $T_N \approx 23$ K reported for 5 SL $MnBi_2Te_4$;[27] however, in both ref 22 and 27, a decrease in the Néel temperature is reported with decreasing thickness. Furthermore, ref 27 reports corrections to the temperature-dependent resistivity with an abrupt downturn in resistivity below T_N, followed by a rapid increase at ≈10 K which they attribute to localization. The abrupt transition observed at similar temperature here in ARPES, along with the QAH effect in $MnBi_2Te_4$ being limited to 6.5 K,[27] suggests that the phase transition responsible for topological order may occur below the Néel temperature (indicating more than one magnetic phase transition) or that the Néel temperature may be lower in these samples than previously thought. Further work is needed to understand this behavior and to understand whether there are spatial variations in the band gap due to magnetic disorder, which has been previously observed in dilute magnetically doped TIs.[16]

CONCLUSIONS

Our results provide an experimental demonstration of the thickness-dependent electronic properties of $MnBi_2Te_4$, from a wide band gap 2D ferromagnet to a QAH insulator with a magnetic band gap in excess of 70 meV. Therefore, $MnBi_2Te_4$ not only offers pathways to realize high temperature QAH effect but also is applicable in designer van der Waals heterostructures for proximity induced magnetization[21] and in the realization of distinct topological phases such as chiral Majorana fermions via coupling to a superconductor.[13]

METHODS

Growth of Ultrathin $MnBi_2Te_4$ on Si(111). Ultrathin $MnBi_2Te_4$ thin films were grown in a UHV MBE chamber and then immediately transferred after growth to an interconnected ARPES chamber at Beamline 10.0.1 (Advanced Light Source (ALS), Lawrence Berkeley National Laboratory, CA). To prepare an atomically flat substrate, a Si(111) wafer was flash-annealed with e-beam heating in order to achieve a (7 × 7) surface reconstruction.

For $MnBi_2Te_4$ film growth, effusion cells were used to evaporate elemental Bi (99.999%) and Mn (99.9%) in an overflux of Te (99.95%). Rates were calibrated with a quartz crystal microbalance. High-quality epitaxial growth of $MnBi_2Te_4$ was achieved by first growing 1 QL of Bi_2Te_3 at 230 °C, and then a bilayer of MnTe was deposited in order to spontaneously form $MnBi_2Te_4$ in a similar manner to the formation of $MnBi_2Se_4$.[32] To reach the desired thickness this recipe was continued by again depositing 1 QL of Bi_2Te_3 followed by a bilayer of MnTe. After growth was completed, the film was annealed at the same temperature in an overflux of Te for 5−10 min to improve crystallinity. RHEED and LEED were used to confirm the (001) single-crystal epitaxial growth across a large area (see Supporting Information Section S1).

Angle-Resolved Photoemission Spectroscopy Measurements and X-ray Photoelectron Spectroscopy. ARPES measurements were carried out at Beamline 10.0.1 of the ALS. Data were recorded using a Scienta R4000 analyzer at temperatures between 8 and 33 K. The total energy resolution was 15−25 meV depending on the beamline slit widths and analyzer settings, and the angular resolution was 0.2°. This resulted in an overall momentum resolution of ≈ 0.01 Å^{-1} for the photoemission kinetic energies measured, with the majority of the measurements carried out at $h\nu = 50$ eV. XPS measurements were carried out at the Soft X-ray Beamline of the Australian Synchrotron using a SPECS Phoibos-150 Spectrometer at room temperature. The Bi 5d, Te 4d, and Mn 3p core levels were measured at photon energies of 100, 350, 850, and 1486 eV. This ensured surface sensitivity for the low photon energy scans at 100 eV, with the higher photon energies used to characterize the depth dependence of the core levels, to confirm there was only $MnBi_2Te_4$ throughout the film. The binding energy scale of all spectra are referenced to the Fermi energy (E_F), determined using either the Fermi edge or 4f core level of an Au reference foil in electrical contact with the sample.

DFT Calculations. We employed DFT calculations as implemented in the Vienna *ab Initio* Simulation Package (VASP) to calculate the electronic structure of 2D $MnBi_2Te_4$.[33] The electron exchange and correlation effects were treated with the Perdew−Burke−Ernzehof (PBE) form of the generalized gradient approximation (GGA).[34] The kinetic energy cutoff for the plane-wave basis was set to 400 eV. We use a 12 × 12 × 1 Γ-centered k-point mesh for sampling the Brillouin zone. The van der Waals interactions in the system is described using the DFT-D3 potential.[35] To treat the strong, on-site Coulombic interactions of localized 3d electrons of Mn, which is inaccurately described by GGA, we used GGA+U approach with the effective Hubbard-like term U set to 4 eV.[36] The electronic bandstructure of 2D $MnBi_2Te_4$ obtained from PBE−GGA was further verified using the hybrid Heyd−Scuseria−Ernzerhof (HSE) hybrid functional.[37]

ASSOCIATED CONTENT

Supporting Information

The Supporting Information is available free of charge at https://pubs.acs.org/doi/10.1021/acsnano.1c03936.

Sample characterization with LEED and RHEED, lattice constant as a function of thickness, X-ray photoelectron spectroscopy of $MnBi_2Te_4$, DFT calculations, effective mass in 2 SL, photon energy dependence of 5 SL, temperature dependence of 5 SL, photon-energy dependent gap of 5 SL, a comparison between four peak and three peak fittings (PDF)

AUTHOR INFORMATION

Corresponding Authors

Mark T. Edmonds − *Monash University, School of Physics and Astronomy, Clayton, Victoria 3800, Australia;* orcid.org/0000-0001-8054-5470; Email: mark.edmonds@monash.edu

Nikhil V. Medhekar − *Monash University, Department of Materials Science and Engineering, Clayton, Victoria 3800, Australia;* orcid.org/0000-0003-3124-4430; Email: nikhil.medhekar@monash.edu

Authors

Chi Xuan Trang − *Monash University, School of Physics and Astronomy, Clayton, Victoria 3800, Australia;* orcid.org/0000-0002-0995-3479

Qile Li − *Monash University, School of Physics and Astronomy, Clayton, Victoria 3800, Australia*

Yuefeng Yin − *Monash University, Department of Materials Science and Engineering, Clayton, Victoria 3800, Australia*

Jinwoong Hwang − *Lawrence Berkeley National Laboratory, Berkeley, California 94720-8099, United States*

Golrokh Akhgar − *Monash University, School of Physics and Astronomy, Clayton, Victoria 3800, Australia*

Iolanda Di Bernardo − *Monash University, School of Physics and Astronomy, Clayton, Victoria 3800, Australia;* orcid.org/0000-0002-2364-5544

Antonija Grubišić-Čabo − *KTH, Applied Physics, Stockholm 114 19, Sweden;* orcid.org/0000-0001-7683-0295

Anton Tadich − *Australian Synchrotron, Clayton, Victoria 3168, Australia*

Michael S. Fuhrer − *Monash University, School of Physics and Astronomy, Clayton, Victoria 3800, Australia;* orcid.org/0000-0001-6183-2773

Sung-Kwan Mo − *Lawrence Berkeley National Laboratory, Berkeley, California 94720-8099, United States;* orcid.org/0000-0003-0711-8514

Complete contact information is available at: https://pubs.acs.org/10.1021/acsnano.1c03936

Author Contributions

#C.X.T., Q.L., and Y.Y. contributed equally to this work. M.T.E. devised the experiments. Q.L., C.X.T., and G.A carried out the MBE growth at Monash University. C. X. T., Q. L., M.T.E., A.G.C., and I.D.B. carried out the MBE growth and ARPES measurements at the ALS with the support from J.H. and S.-K.M. I.D.B. carried out the STM measurements at Monash University. The DFT calculations were carried out by Y.Y., and N.M. C.X.T., Q.L., and M.T.E. composed the manuscript. All authors read and contributed feedback to the manuscript.

Notes

Preprint version of this manuscript: Trang, C. X.; Li, Q.; Yin, Y.; Hwang, J.; Akhgar, G.; Di Bernardo, I.; Grubišić-Čabo, A.; Tadich, A.; Fuhrer, M. S.; Mo, S.-K. et al. Crossover From 2D Ferromagnetic Insulator to Wide Bandgap QuantumAnomalous Hall Insulator in Ultra-Thin $MnBi_2Te_4$. *arXiv.org (Materials Science)*,March 17, 2021, arXiv:2009.06175v2, https://arxiv.org/abs/2009.06175.

The authors declare no competing financial interest.

ACKNOWLEDGMENTS

M.T.E. was supported by ARC DECRA fellowship DE160101157. M.T.E., C.X.T., Q.L., Y. Y., I.D.B., G.A., N.V.M., and M.S.F. acknowledge funding support from CE170100039. M.T.E. and C.X.T. acknowledge travel funding provided by the International Synchrotron Access Program (ISAP) managed by the Australian Synchrotron, part of ANSTO, and funded by the Australian Government. M.T.E., C.X.T., and Q.L. acknowledge funding support from ARC Centre for Future Low Energy Electronics Technologies (FLEET). Y.Y. and N.V.M. are thankful for the computational support provided by the Monash Computing Cluster, the National Computing Infrastructure and the Pawsey Supercomputing Facility. This research used resources of the Advanced Light Source, which is a DOE Office of Science User Facility under contract no. DE-AC02-05CH11231. Part of this research was also undertaken on the Soft X-ray beamline at the Australian Synchrotron, part of ANSTO.

REFERENCES

(1) Fu, L.; Kane, C. L.; Mele, E. J. Topological Insulators in Three Dimensions. *Phys. Rev. Lett.* **2007**, *98* (10), 106803.

(2) Hasan, M. Z.; Kane, C. L. Colloquium: Topological Insulators. *Rev. Mod. Phys.* **2010**, *82* (4), 3045.

(3) Chen, Y. L.; Analytis, J. G.; Chu, J.-H.; Liu, Z. K.; Mo, S.-K.; Qi, X. L.; Zhang, H. J.; Lu, D. H.; Dai, X.; Fang, Z.; Zhang, S. C.; Fisher, I. R.; Hussain, Z.; Shen, Z.-X. Experimental Realization of a Three-Dimensional Topological Insulator, Bi_2Te_3. *Science* **2009**, *325* (5937), 178.

(4) Li, Y.-Y.; Li, Y.-Y.; Wang, G.; Zhu, X.-G.; Liu, M.-H.; Ye, C.; Chen, X.; Wang, Y.-Y.; He, K.; Wang, L.-L.; et al. Intrinsic Topological Insulator Bi_2Te_3 Thin Films on Si and Their Thickness Limit. *Adv. Mater.* **2010**, *22* (36), 4002.

(5) Zhang, Y.; He, K.; Chang, C.-Z.; Song, C.-L.; Wang, L.-L.; Chen, X.; Jia, J.-F.; Fang, Z.; Dai, X.; Shan, W-Y; Shen, S.-Q.; Niu, Q.; Qi, X.-L.; Zhang, S.-C.; Ma, X.-C.; Xue, Q.-K. Crossover of the Three-Dimensional Topological Insulator Bi_2Se_3 to the Two-Dimensional Limit. *Nat. Phys.* **2010**, *6*, 584.

(6) Chen, Y. L.; Chu, J.-H.; Analytis, J. G.; Liu, Z. K.; Igarashi, K.; Kuo, H.-H.; Qi, X. L.; Mo, S. K.; Moore, R. G.; Lu, D. H.; Hashimoto, M.; Sasagawa, T.; Zhang, S. C.; Fisher, I. R.; Hussain, Z.; Shen, Z. X. Massive Dirac Fermion on the Surface of a Magnetically Doped Topological Insulator. *Science* **2010**, *329* (5992), 659.

(7) Rienks, E. D. L.; Wimmer, S.; Sánchez-Barriga, J.; Caha, O.; Mandal, P. S.; Růžička, J.; Ney, A.; Steiner, H.; Volobuev, V. V.; Groiss, H.; Albu, M.; Kothleitner, G.; Michalička, J.; Khan, S. A.; Minár, J.; Ebert, H.; Bauer, G.; Freyse, F.; Varykhalov, A.; Rader, O.; Springholz, G. Large Magnetic Gap at the Dirac Point in $Bi_2Te_3/MnBi_2Te_4$ Heterostructures. *Nature* **2019**, *576*, 423.

(8) Yu, R.; Zhang, W.; Zhang, H.-J.; Zhang, S.-C.; Dai, X.; Fang, Z. Quantized Anomalous Hall Effect in Magnetic Topological Insulators. *Science* **2010**, *329* (5987), 61.

(9) Chang, C.-Z.; Zhang, J.; Feng, X.; Shen, J.; Zhang, Z.; Guo, M.; Li, K.; Ou, Y.; Wei, P.; Wang, L.-L.; Ji, Z.-Q.; Feng, Y.; Ji, S.; Chen, X.; Jia, J.; Dai, X.; Fang, Z.; Zhang, S.-C.; He, K.; Wang, Y.; et al. Experimental Observation of the Quantum Anomalous Hall Effect in a Magnetic Topological Insulator. *Science* **2013**, *340* (6129), 167.

(10) Chang, C.-Z.; Zhao, W.; Kim, D. Y.; Zhang, H.; Assaf, B. A.; Heiman, D.; Zhang, S.-C.; Liu, C.; Chan, M. H. W.; Moodera, J. S. High-Precision Realization of Robust Quantum Anomalous Hall State in a Hard Ferromagnetic Topological Insulator. *Nat. Mater.* **2015**, *14*, 473.

(11) Gambardella, P.; Dallmeyer, A.; Maiti, K.; Malagoli, M. C.; Eberhardt, W.; Kern, K.; Carbone, C. Ferromagnetism in One-Dimensional Monatomic Metal Chains. *Nature* **2002**, *416*, 301.

(12) Tokura, Y.; Yasuda, K.; Tsukazaki, A. Magnetic Topological Insulators. *Nature Rev. Phys.* **2019**, *1*, 126.

(13) He, Q. L.; Pan, L.; Stern, A. L.; Burks, E. C.; Che, X.; Yin, G.; Wang, J.; Lian, B.; Zhou, Q.; Choi, E. S.; Murata, K.; Kou, X.; Chen, Z.; Nie, T.; Shao, Q.; Fan, Y.; Zhang, S.-C.; Liu, K.; Xia, J.; Wang, K. L. Chiral Majorana Fermion Modes in a Quantum Anomalous Hall Insulator−Superconductor Structure. *Science* **2017**, *357* (6348), 294.

(14) Li, R.; Wang, J.; Qi, X.-L.; Zhang, S.-C. Dynamical Axion Field in Topological Magnetic Insulators. *Nat. Phys.* **2010**, *6*, 284.

(15) Liu, C.; Wang, Y.; Li, H.; Wu, Y.; Li, Y.; Li, J.; He, K.; Xu, Y.; Zhang, J.; Wang, Y. Robust Axion Insulator and Chern Insulator Phases in a Two-Dimensional Antiferromagnetic Topological Insulator. *Nat. Mater.* **2020**, *19*, 522.

(16) Lee, I.; Kim, C. K.; Lee, J.; Billinge, S. J. L.; Zhong, R.; Schneeloch, J. A.; Liu, T.; Valla, T.; Tranquada, J. M.; Gu, G.; Davis, J. C. S. Imaging Dirac-Mass Disorder from Magnetic Dopant Atoms in the Ferromagnetic Topological Insulator $Cr_x(Bi_{0.1}Sb_{0.9})_{2-x}Te_3$. *Proc. Natl. Acad. Sci. U. S. A.* **2015**, *112* (5), 1316.

(17) Ou, Y.; Ou, Y.; Liu, C.; Jiang, G.; Feng, Y.; Zhao, D.; Wu, W.; Wang, X.-X.; Li, W.; Song, C.; et al. Enhancing the Quantum Anomalous Hall Effect by Magnetic Codoping in a Topological Insulator. *Adv. Mater.* **2018**, *30* (1), 1703062.

(18) Mogi, M.; Yoshimi, R.; Tsukazaki, A.; Yasuda, K.; Kozuka, Y.; Takahashi, K. S.; Kawasaki, M.; Tokura, Y. Magnetic Modulation Doping in Topological Insulators toward Higher-Temperature Quantum Anomalous Hall Effect. *Appl. Phys. Lett.* **2015**, *107*, 182401.

(19) Li, J.; Li, Y.; Du, S.; Wang, Z.; Gu, B.-L.; Zhang, S.-C.; He, K.; Duan, W.; Xu, Y. Intrinsic Magnetic Topological Insulators in van der Waals Layered $MnBi_2Te_4$-Family Materials. *Sci. Adv.* **2019**, *5* (6), No. eaaw5685.

(20) Zhang, D.; Shi, M.; Zhu, T.; Xing, D.; Zhang, H.; Wang, J. Topological Axion States in the Magnetic Insulator $MnBi_2Te_4$ with the Quantized Magnetoelectric Effect. *Phys. Rev. Lett.* **2019**, *122* (20), 206401.

(21) Otrokov, M. M.; Menshchikova, T. V.; Vergniory, M. G.; Rusinov, I. P.; Vyazovskaya, A. Yu.; Koroteev, Y. M.; Bihlmayer, G.; Ernst, A.; Echenique, P. M.; Arnau, A.; Chulkov, E. V. Highly-Ordered Wide Bandgap Materials for Quantized Anomalous Hall and Magnetoelectric Effects. *2D Mater.* **2017**, *4* (2), No. 025082.

(22) Otrokov, M. M.; Rusinov, I. P.; Blanco-Rey, M.; Hoffmann, M.; Vyazovskaya, A. Yu.; Eremeev, S. V.; Ernst, A.; Echenique, P. M.; Arnau, A.; Chulkov, E. V. Unique Thickness-Dependent Properties of the van der Waals Interlayer Antiferromagnet $MnBi_2Te_4$ Films. *Phys. Rev. Lett.* **2019**, *122* (10), 107202.

(23) Lee, S. H.; Zhu, Y.; Wang, Y.; Miao, L.; Pillsbury, T.; Yi, H.; Kempinger, S.; Hu, J.; Heikes, C. A.; Quarterman, P.; et al. Spin Scattering and Noncollinear Spin Structure-Induced Intrinsic Anomalous Hall Effect in Antiferromagnetic Topological Insulator $MnBi_2Te_4$. *Phys. Rev. Research* **2019**, *1* (1), No. 012011(R).

(24) Vidal, R. C.; Bentmann, H.; Peixoto, T. R. F.; Zeugner, A.; Moser, S.; Min, C.-H.; Schatz, S.; Kißner, K.; Ünzelmann, M.; Fornari, C. I.; et al. Surface States and Rashba-Type Spin Polarization in Antiferromagnetic $MnBi_2Te_4$ (0001). *Phys. Rev. B: Condens. Matter Mater. Phys.* **2019**, *100* (12), 121104.

(25) Otrokov, M. M.; Klimovskikh, I. I.; Bentmann, H.; Estyunin, D.; Zeugner, A.; Aliev, Z. S.; Gaß, S.; Wolter, A. U. B.; Koroleva, A. V.; Shikin, A. M.; Blanco-Rey, M.; Hoffmann, M.; Rusinov, I. P.; Vyazovskaya, A. Yu.; Eremeev, S. V.; Koroteev, Y. M.; Kuznetsov, V. M.; Freyse, F.; Sánchez-Barriga, J.; Amiraslanov, I. R.; et al. Prediction and Observation of an Antiferromagnetic Topological Insulator. *Nature* **2019**, *576*, 416.

(26) Zeugner, A.; Nietschke, F.; Wolter, A. U. B.; Gaß, S.; Vidal, R. C.; Peixoto, T. R. F.; Pohl, D.; Damm, C.; Lubk, A.; Hentrich, R.; Moser, S. K.; Fornari, C.; Min, C. H.; Schatz, S.; Kißner, K.; Ünzelmann, M.; Kaiser, M.; Scaravaggi, F.; Rellinghaus, B.; Nielsch, K.; et al. Chemical Aspects of the Candidate Antiferromagnetic Topological Insulator $MnBi_2Te_4$. *Chem. Mater.* **2019**, *31* (8), 2795.

(27) Deng, Y.; Yu, Y.; Shi, M. Z.; Guo, Z.; Xu, Z.; Wang, J.; Chen, X. H.; Zhang, Y. Quantum Anomalous Hall Effect in Intrinsic Magnetic Topological Insulator $MnBi_2Te_4$. *Science* **2020**, *367* (6480), 895.

(28) Gong, Y.; Guo, J.; Li, J.; Zhu, K.; Liao, M.; Liu, X.; Zhang, Q.; Gu, L.; Tang, L.; Feng, X.; Zhang, D.; Li, W.; Song, C.; Wang, L.; Yu, P.; Chen, X.; Wang, Y.; Yao, H.; Duan, W.; Xu, Y.; et al. Experimental Realization of an Intrinsic Magnetic Topological Insulator. *Chin. Phys. Lett.* **2019**, *36* (7), No. 076801.

(29) Lee, D. S.; Kim, T.-H.; Park, C.-H.; Chung, C.-Y.; Lim, Y. S.; Seo, W.-S.; Park, H.-H. Crystal Structure, Properties and Nanostructuring of a New Layered Chalcogenide Semiconductor, Bi_2MnTe_4. *CrystEngComm* **2013**, *15*, 5532.

(30) Perdew, J. P.; Yang, W.; Burke, K.; Yang, Z.; Gross, E. K. U.; Scheffler, M.; Scuseria, G. E.; Henderson, T. M.; Zhang, I. Y.; Ruzsinszky, A.; Peng, H.; Sun, J.; Trushin, E.; Görling, A. Understanding Band Gaps of Solids in Generalized Kohn−Sham Theory. *Proc. Natl. Acad. Sci. U. S. A.* **2017**, *114* (11), 2801.

(31) Webster, L.; Yan, J.-A. Strain-Tunable Magnetic Anisotropy in Monolayer $CrCl_3$, $CrBr_3$, and CrI_3. *Phys. Rev. B: Condens. Matter Mater. Phys.* **2018**, *98* (14), 144411.

(32) Hirahara, T.; Eremeev, S. V.; Shirasawa, T.; Okuyama, Y.; Kubo, T.; Nakanishi, R.; Akiyama, R.; Takayama, A.; Hajiri, T.; Ideta, S.; Matsunami, M.; Sumida, K.; Miyamoto, K.; Takagi, Y.; Tanaka, K.; Okuda, T.; Yokoyama, T.; Kimura, S.; Hasegawa, S.; Chulkov, E. V. Large-Gap Magnetic Topological Heterostructure Formed by Subsurface Incorporation of a Ferromagnetic Layer. *Nano Lett.* **2017**, *17*, 3493.

(33) Kresse, G.; Furthmüller, J. Efficiency of *ab Initio* Total Energy Calculations for Metals and Semiconductors Using a Plane-Wave Basis Set. *Comput. Mater. Sci.* **1996**, *6*, 15.

(34) Perdew, J. P.; Burke, K.; Ernzerhof, M. Generalized Gradient Approximation Made Simple. *Phys. Rev. Lett.* **1996**, *77*, 3865.

(35) Grimme, S.; Antony, J.; Ehrlich, S.; Krieg, H. A. Consistent and Accurate *ab Initio* Parametrization of Density Functional Dispersion Correction (DFT-D) for the 94 Elements H-Pu. *J. Chem. Phys.* **2010**, *132*, 154104.

(36) Dudarev, S. L.; Botton, G. A.; Savrasov, S. Y.; Humphreys, C. J.; Sutton, A. P. Electron-Energy-Loss Spectra and the Structural Stability of Nickel Oxide: An LSDA+U Study. *Phys. Rev. B: Condens. Matter Mater. Phys.* **1998**, *57*, 1505.

(37) Heyd, J.; Scuseria, G. E.; Ernzerhof, M. Hybrid Functionals Based on a Screened Coulomb Potential. *J. Chem. Phys.* **2003**, *118*, 8207.